

Imaging orbital Rashba induced charge transport anisotropy

Eylon Persky,^{1,2} Xi Wang,^{1,2} Giacomo Sala,³ Thierry C. van Thiel,^{4,5} Edouard Lesne,^{4,5} Alexander Lau,⁶ Mario Cuoco,⁷ Marc Gabay,⁸ Carmine Ortix,^{9,*} Andrea D. Caviglia,^{3,†} and Beena Kalisky^{1,2,‡}

¹*Department of Physics, Bar-Ilan University, Ramat-Gan 5290002, Israel*

²*Institute of Nanotechnology and Advanced Materials, Bar-Ilan University, Ramat-Gan 5290002, Israel*

³*Department of Quantum Matter Physics, University of Geneva,*

24 Quai Ernest Ansermet, CH-1211 Geneva, Switzerland

⁴*Kavli Institute of Nanoscience, Delft University of Technology, Lorentzweg 1, 2628CJ Delft, Netherlands*

⁵*Max Planck Institute for Chemical Physics of Solids, 01187 Dresden, Germany*

⁶*International Research Centre MagTop, Institute of Physics,
Polish Academy of Sciences, Aleja Lotników 32/46, PL-02668 Warsaw, Poland*

⁷*Consiglio Nazionale delle Ricerche, CNR-SPIN, Italy*

⁸*Laboratoire de Physique des Solides, Université Paris-Saclay, CNRS UMR 8502, Orsay, France*

⁹*Dipartimento di Fisica "E. R. Caianiello", Università di Salerno, IT-84084 Fisciano, Italy*

Identifying orbital textures and their effects on the electronic properties of quantum materials is a critical element in developing orbitronic devices. However, orbital effects are often entangled with the spin degree of freedom, making it difficult to uniquely identify them in charge transport phenomena. Here, we present a combination of scanning superconducting quantum interference device (SQUID) current imaging, global transport measurements, and theoretical analysis, that reveals a direct contribution of orbital textures to the linear charge transport of 2D systems. Specifically, we show that in the $\text{LaAlO}_3/\text{SrTiO}_3$ interface, which lacks both rotation and inversion symmetries, an anisotropic orbital Rashba coupling leads to conductivity anisotropy in zero magnetic field. We experimentally demonstrate this result by locally measuring the conductivity anisotropy, and correlating its appearance to the non-linear Hall effect, showing that the two phenomena have a common origin. Our results lay the foundations for an all-electrical probing of orbital currents in two-dimensional systems.

INTRODUCTION

The multi-orbital nature of oxide interfaces [1–3], combined with their low crystalline symmetry, enables a plethora of quantum phenomena, such as quantum geometry induced non-linear transport [4–6] and unconventional superconductivity [7, 8]. The gate tunability of these properties is particularly promising as a platform to engineer novel devices or investigate transitions between different electronic phases. One example is the orbital Hall effect (OHE) [9] and its surface counterpart, the orbital Rashba-Edelstein effect (OREE), where a charge current generates a transverse flow of orbital angular momentum. These effects are analogous to the spin Hall effect and the spin Rashba-Edelstein effect, respectively. Through this effect, the orbital degree of freedom can be used to generate and detect information [10]. Both the OREE and the OHE can be directly related to the existence of momentum-space orbital textures [11]. In non-centrosymmetric low-dimensional materials these textures arise from a linear coupling, known as the orbital Rashba coupling [12, 13], between the crystalline momentum \mathbf{k} and the orbital angular momentum \mathbf{L} . The coupling strength can be controlled using electrostatic fields, setting the stage for a controlled generation of orbital currents. This provides a strong motivation to detect orbital textures and identify their sources in materials with low crystalline symmetry. One approach is to analyze how such couplings affect the charge transport properties of

the material. For example, Rashba SOC gives rise to weak anti-localization, with signatures such as positive magnetoresistance [14] and (non) linear transport due to band geometric properties [4, 6, 15, 16]. In contrast, the signatures of orbital effects are often difficult to detect, because they are weak, or because multiple microscopic mechanisms can explain the observed experimental results. In these cases, new tools, or a combination of several probes, are required to pinpoint the cause of transport anomalies.

A notable example is the transport anisotropy in $\text{LaAlO}_3/\text{SrTiO}_3$. At low temperatures, the tetragonal distortion of SrTiO_3 breaks the rotational symmetry, allowing for anisotropy in the DC, zero-field charge transport. Indeed, experiments generally measure such anisotropy [17–22], but its source has been disputed. Several intrinsic mechanisms can generate anisotropy, including Fermi surface warping and the orbital Rashba coupling. The latter option, which further requires inversion symmetry breaking, is particularly interesting because it gives rise to transverse orbital currents, which are useful for device applications [23, 24]. In the superconducting state, such orbital mixing could also lead to new pairing channels [25]. However, the large variability in reported results, as well as several scanning probe experiments [19, 20, 26–31], suggested that the origin could be extrinsic. Namely, tetragonal domains of different orientations can have different properties [29, 30], or the walls between the structural domains could host highly-

conducting quasi-1D channels [32–34] that manifest as anisotropy in the global transport measurement. Determining the origin of anisotropy is crucial to interpreting quantum transport measurements in SrTiO₃-based interfaces, and for harnessing their properties for device applications.

In this work, we use a combination of global transport measurements, local current imaging and theoretical analysis to associate the origin of transport anisotropy in (111) oriented LaAlO₃/SrTiO₃ interface with the orbital Rashba coupling. Firstly, we locally probe the current flow at the interface and show direct and unambiguous evidence that the anisotropy is an intrinsic property of the interface. Secondly, we measure the non-linear Hall effect, whose presence is a direct indicator of inversion symmetry breaking. We find a correlation between the temperature dependence of the two effects, which suggests that they have a common origin. Finally, we interpret these results using a $\mathbf{k} \cdot \mathbf{p}$ model of the band structure, which allows us to identify the anisotropic orbital Rashba coupling - a linear-in-momentum, anisotropic mixing of the t_{2g} orbitals - as the leading term responsible for both effects. Our results provide a new platform for exploring orbital effects and controlling the orbital degree of freedom in various systems.

RESULTS

Intrinsic anisotropy in (111) LaAlO₃/SrTiO₃

To distinguish between intrinsic and extrinsic origins of transport anisotropy, we used a local probe, a scanning superconducting quantum interference device (SQUID), to directly image the current flow at the interface. Scanning SQUID was previously used to study (001)-based interfaces, revealing that current density is spatially inhomogeneous, and that the inhomogeneity is correlated with the tetragonal domain structure of the SrTiO₃ substrate [26]. While these observations might point to an extrinsic source - the network of domains or domain walls - this determination cannot be made based on existing data. Specifically, it was difficult to distinguish between enhanced current density on entire domains versus domain boundaries, and to relate these to the components of the conductivity tensor. Here we study the (111) oriented interface, in which we found that domains tend to be wider, and the tiling rules of the domains enable us to determine their orientations unambiguously.

Figure 1 shows results from a triangle patterned (111)-oriented LaAlO₃/SrTiO₃ device (Methods). We observed current density modulations (Figure 1b), across the device. The modulations changed after a thermal cycle above 105 K, confirming that they originate from the STO tetragonal domains (Fig. S1). Based on the tiling rules, we determined the orientation of the domains to

be along the [100] and [010] axes. The modulations were over 10 μm wide strips which terminate at needle-like shapes. The modulations reveal a surprising dependence on the device geometry: On the left side of the triangle, the current density along [112] is larger on X domains than on Y domains but lower on the right side. The change coincides with a reflection of \mathbf{J} with respect to the [112] crystallographic direction. This relationship between the current direction and the modulation has not been previously reported in the (001) interface. We thus associate the modulations with a change in the properties of the X and Y domains, rather than a domain-boundary effect. Figs. S2, S3 and S4 show data from 3 additional devices with various geometries and domain patterns.

To understand the difference between the (001) and (111) interfaces, we note that at (001) interfaces, (001)-oriented domains (Z-domains) have a C_{4v} symmetry, while (100) and (010) domains (X,Y-domains) have C_{2v} symmetry. Therefore, in (001) interfaces, the conductivity of Z domains is intrinsically isotropic, and is described by a single scalar. For X and Y domains, the conductivity tensor has a symmetry-allowed anisotropy, but it is diagonal with respect to the (100) and (010) directions. The situation changes in (111) oriented interfaces. All domains have the same crystalline symmetry group, C_s , which admits an anisotropic conductivity tensor with principal directions that do not coincide with the crystallographic directions. Denoting the current density as the 2D vector

$$\mathbf{J} = \begin{pmatrix} J_{[1\bar{1}0]} \\ J_{[11\bar{2}]} \end{pmatrix}, \quad (1)$$

The conductivity tensor for Z-domains is anisotropic but diagonal,

$$\sigma^Z = \begin{pmatrix} \sigma_{xx} & 0 \\ 0 & \sigma_{yy} \end{pmatrix}, \quad (2)$$

while the X and Y domain conductivities are related by a 120° rotation,

$$\sigma^{X,Y} = \frac{1}{4} \begin{pmatrix} \sigma_{xx} + 3\sigma_{yy} & \pm\sqrt{3}(\sigma_{xx} - \sigma_{yy}) \\ \pm\sqrt{3}(\sigma_{xx} - \sigma_{yy}) & \sigma_{yy} + 3\sigma_{xx} \end{pmatrix}. \quad (3)$$

Note that the off-diagonal elements are non-zero (in zero magnetic field) only if the conductivity is anisotropic ($\sigma_{xx} \neq \sigma_{yy}$).

The off-diagonal components of the conductivity are at the origin of the reversed modulations observed in the data. In Fig. 1c, we schematically show an anisotropic Fermi surface with corresponding direction-dependent Fermi velocities that yield a fast and a slow direction. The current density \mathbf{J} is increased when the electric field is aligned with the fast direction of the Fermi surface, which causes the modulations. On the left side of the device, this alignment is greater in x domains. As the current flow is reflected about the [112] direction, due to

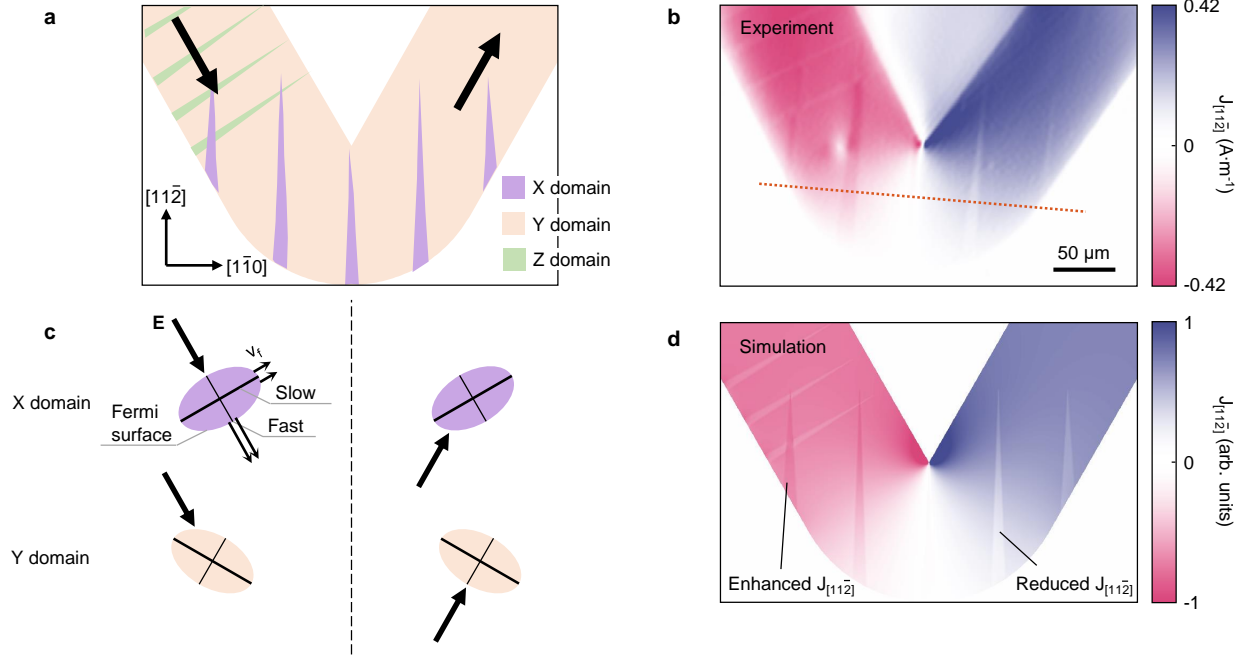


FIG. 1: Modulation reversal upon reflection of the current flow. (a) Schematic of a triangle-shaped device with an X-Y domain pattern. The current density is reflected around the $[11\bar{2}]$ direction upon flowing across the device. (b) A scanning SQUID image of the current flow in a (111)-oriented device. The current is modulated over the domain pattern: on the left side of the device, current density on X domains is larger than on Y-domains. This trend is reversed on the right side of the device, coinciding with a reflection of the overall current density. The modulation strength is about 8%. (c) Schematic of the Fermi surface at the X and Y domains, showing the direction of the electric field on the two sides of the device. On the left, the electric field is aligned with the fast direction on X domains, resulting in increased current density. This is reversed on the right side of the device. (d) Simulated current density map of the device, where an anisotropic conductivity tensor was introduced in order to account for the reversed modulations.

the triangle shape of the device, E is aligned with the fast direction in the Y domains, thus reversing the current density modulation. Fig. 1d shows finite element simulations (Methods) of the current density in such geometry, which confirm that the modulation trends are reversed. Furthermore, domains with different (but isotropic) conductivity would lead to modulations that do not reverse sign upon reflection of the device (Methods). Thus, observing this change of sign is a direct measure of the intrinsic conductivity anisotropy of an individual domain.

Correlation between anisotropy and inversion symmetry breaking

To investigate the origin of the anisotropy, we studied the temperature dependence of the modulations. Fig. 2a,b shows how the current density modulations decreased upon increasing the temperature, until disappearing at 35 K. This temperature dependence is consistent with previous observations on the (001) interface [26]. It is important to note that even though the do-

main exists already at 105 K, and the crystalline symmetry allows anisotropy to exist below 105 K, it is not observed in the range $35 < T < 105$, suggesting there is another mechanism which generates, or enhances the anisotropy at lower temperatures.

There are several possible mechanisms. Scattering can smear the effect at elevated temperatures, explaining the gradual change in the signal. In SrTiO_3 , the scattering could be suppressed at low temperatures due to the large dielectric constant. Alternatively, the appearance of modulations only below 35 K can suggest that the modulations are caused by a structural change occurring at this temperature. Bulk SrTiO_3 shows an increased dielectric permittivity below 40 K, signalling an incipient ferroelectric state [35]. This quantum paraelectric phase significantly enhances the inversion symmetry breaking that is already present at the interface [36].

To understand the source of the anisotropy, we further studied the symmetry of the system by measuring the nonlinear Hall effect. Observing nonlinear transport is a direct consequence of inversion symmetry breaking. Furthermore, previous work on oxide interfaces, which stud-

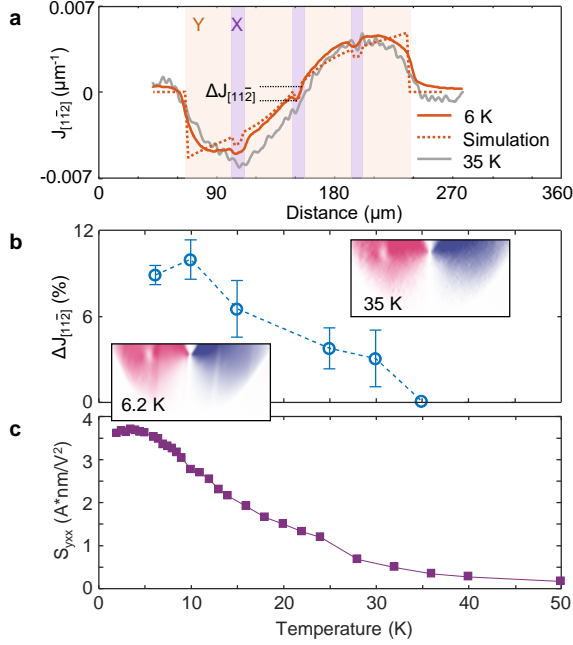


FIG. 2: Temperature and carrier density dependence of the anisotropy. (a) Line-cut along the dashed line in Fig. 1b, along with a line cut of the simulated current densities. The modulation is 10%. The gray line is a line-cut taken at the same location but at 35 K. The current densities are normalized by the applied current. (b) Temperature dependence of the current density modulations shown in panel a. The modulation of current density decreases with temperature and disappears near 35 K. Insets: current density maps at 6 K and 35 K. (c) Temperature dependence of the non-linear conductivity, measured at zero magnetic field, showing similar onset temperature to the anisotropy.

ied the magnetic field dependence of the nonlinear Hall [4], associated it with a Berry curvature dipole, which indicates the presence of an orbital Rashba coupling. We measured the temperature dependence of the nonlinear Hall conductivity on a four-point device on the same sample, and found that it onsets at 40 K (Fig. 2c). This temperature is in line with previous work showing the same characteristic temperature [4]. Remarkably, both the linear conductivity anisotropy and the nonlinear Hall conductivity onset at the same temperature, even though the corresponding crystalline symmetries (rotation and inversion) are already broken at much higher temperatures. This correlation indicates that the two effects share a common origin.

$\mathbf{k} \cdot \mathbf{p}$ model and sources of anisotropy

We use a $\mathbf{k} \cdot \mathbf{p}$ model to analyze the symmetry allowed terms and their contribution to the transport anisotropy. Above 105 K, the system retains its trigonal symmetry, and belongs to the C_{3v} symmetry group. At zero magnetic field, the spin degree of freedom does not contribute to the linear conductivity [37]. We therefore consider a spinless Hamiltonian, which contains the following symmetry-allowed terms: (1) Splitting between the a_{1g} singlet and the e_g^π doublet due to the trigonal field, (2) $|\mathbf{k}|^2$ terms that account for the trigonal Fermi surface warping. They give rise to an orbital-dependent effective mass, as observed in ARPES experiments [38] and (3) k -linear terms that are allowed by the broken inversion symmetry. These terms, which are proportional to $\mathbf{k} \cdot \mathbf{L}$ where \mathbf{L} are the angular momentum matrices, are the orbital Rashba coupling. They mix the orbital bands and give rise to transverse orbital currents and Berry curvature dipoles.

Below 105 K, the rotational symmetry is broken, reducing the symmetry group to C_s and enabling a plethora of new terms in the Hamiltonian. These terms can be casted into three categories (Methods): (4) splitting of the e_g^π bands, (5) an anisotropic and orbital dependent effective mass (terms proportional to k_x^2 or k_y^2) and [39–42] (6) an anisotropic orbital Rashba coupling (linear in k_x and k_y).

The correlation between the non-linear Hall effect (broken inversion) and the anisotropic linear transport (broken rotation) suggests that the two effects are intertwined. Particularly, we expect the orbital Rashba terms to change strongly at 40 K, as indicated by the non-linear Hall. Figure 3a shows the band structure obtained by fitting to photoemission data from a (111) SrTiO_3 surface [38]. Since the ARPES data fits well to an isotropic model, it provides upper bounds on the contributions from the C_s terms discussed above. To account for the tetragonal distortion, we only include a small splitting (1 meV) of the e_g^π bands. Figure 3a-c shows the resulting band structure and the corresponding Fermi surfaces at carrier densities relevant to our experiment (Fig. S7). The band structure has several important features. Firstly, at low densities it is dominated by the orbital Rashba coupling, which gives rise to the two shifted parabolic features in the lowest bands. Note that at these low energies, the Fermi surface does not show significant tetragonal warping (Fig. 3b), but is strongly anisotropic. At higher energies the warping becomes significant. Notably, the anisotropy in the higher e_g^π bands is opposite to that of the a_{1g} band (Fig. 3a). Correspondingly, the transport anisotropy computed using the Boltzmann formalism (see Methods) is non-monotonic and is stronger at low densities (Fig. 3d). This matches the behavior observed in experiment over the smaller (experimentally

attainable) range of densities (Fig. S6.)

To assess the contribution of Fermi surface warping to the transport anisotropy, we repeated the calculation without including the orbital Rashba effect. The resulting anisotropy was zero at low carrier densities and varied monotonically and quadratically with increasing densities, reflecting the contributions from the quadratic terms. These results indicate that the tetragonal splitting of the e_g^π bands on its own is not sufficient to explain the anisotropy observed in the experiment. While an anisotropic quadratic (mass) term is allowed, and can result in a non-monotonic dependence on the carrier density, the combination of the SQUID images, non-linear Hall effect, temperature and gate dependence indicate that the anisotropy is correlated with the broken inversion symmetry, consistent with the calculations we present, that indicate that the orbital Rashba coupling greatly enhances the anisotropy at low energies.

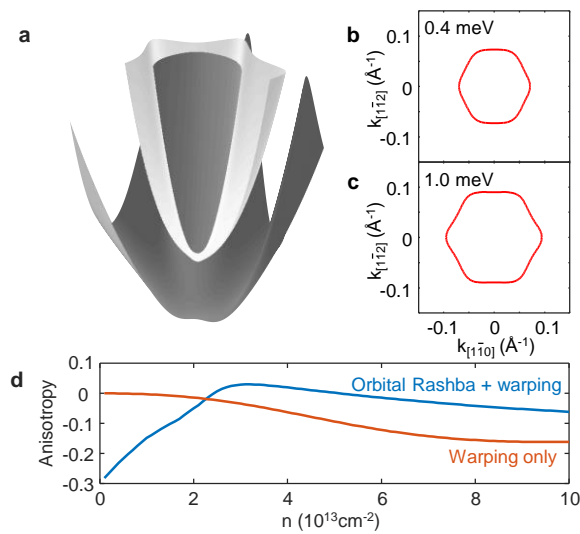


FIG. 3: The anisotropic band structures of (111) $\text{LaAlO}_3/\text{SrTiO}_3$, and carrier density dependence of the anisotropy. (a) The band structure calculated from an effective $\mathbf{k} \cdot \mathbf{p}$ model, showing effects of the orbital Rashba coupling (lateral splitting of the lowest band), Fermi surface warping (flower-like shape at higher energies) and the tetragonal splitting of the e_g^π bands. (b,c) The Fermi surfaces 0.4 meV and 1 meV, showing the anisotropy at low energies, where the band structure is still dominated by the linear (Rashba) terms. (d) Calculated anisotropy as a function of the carrier density with and without including the orbital Rashba coupling.

DISCUSSION

In this work, we show that momentum space orbital textures can be probed by charge transport by lower-

ing the crystalline symmetry. Specifically, the character of the orbital Rashba coupling in the absence of rotational symmetries results in a specific intra-atomic contribution to the orbital Hall effect that is absent in more symmetric crystalline environments. This provides a direct correspondence between charge transport anisotropy and the occurrence of orbital currents causing the OHE. We developed an approach to explore the anisotropy by extracting it from local measurements of the current density, and demonstrated it on (111) $\text{LaAlO}_3/\text{SrTiO}_3$.

In LAO/STO, spin-orbit coupling plays an important role in determining the band structure and electronic behavior [43–47]. The zero-field intrinsic anisotropy uncovered here demonstrates our ability to separate the orbital and spin contributions to transport and identify new features in the band structure. Furthermore, the local measurements enabled us to study the interplay between the orbital currents and the crystalline tetragonal domain patterns. We identified them as the source of the current density modulations previously observed in LAO/STO [19, 20, 26, 27, 31, 32]. We showed that the modulations are caused by anisotropic conductivity, whose principle axes are rotated across different domains.

More generally, our results indicate that by choosing the appropriate crystalline symmetry, orbital currents can be identified by measuring transport anisotropy. This task can be accomplished via various local techniques [48–52] and also through measurements of the global transport anisotropy. Uniquely identifying orbital Hall currents, for example, has been a challenging task because their signatures are similar to spin Hall currents, and therefore limited to systems with low spin-orbit coupling [53, 54]. Our approach offers a way to disentangle the spin and orbital contributions, thereby allowing the study of orbital phenomena in materials with strong SOC.

Finally, we note that the orbital effects we observed in $\text{LaAlO}_3/\text{SrTiO}_3$ are closely associated with the low-temperature transitions of SrTiO_3 . However, a similar low-symmetry structure could be engineered at room temperature by breaking the rotation and inversion symmetries using epitaxial strain and ferroelectric layers. This engineering of orbital-induced anisotropy is relevant not only to complex oxide interfaces. It applies to other orbitronics material candidates, including light and heavy elemental metals and van der Waals heterostructures. The theoretical model and experimental techniques presented here provide an effective platform to characterize the orbital degrees of freedom in these systems.

MATERIALS AND METHODS

Sample growth and device fabrication

To synthesize the $\text{LaAlO}_3/\text{SrTiO}_3$ heterostructure, a commercially available (111) SrTiO_3 substrate with a Ti-rich surface was pasted onto a metal holder and heated to 740°C , at a rate of $15^\circ\text{C min}^{-1}$ in an O_2 pressure of 6×10^{-5} mbar. An 11 unit cell thick LaAlO_3 layer was subsequently grown through pulsed-laser deposition, using a 248 nm KrF excimer laser at a 1 Hz repetition rate and a fluence of 1 J cm^{-2} . The sample surface was monitored during the growth using in-situ reflection high-energy electron spectroscopy (RHEED).

Device geometries were defined by RF-sputtering a HfO_2 hard mask in areas meant to remain insulating, prior to the growth of the LaAlO_3 layer. The hard mask was defined by electron-beam lithography, using a double-layer PMMA liftoff resist stack.

Imaging currents with scanning SQUID microscopy

The sample was glued on a conductive surface and electrical contacts made by ultrasonic wire bonding. A back gate voltage was applied between the interface and the metallic sample holder. To locally measure the current density, an alternating current (34 μA RMS, frequency 1163 Hz for the triangle-shaped device shown in Fig 1; 40 μA RMS, frequency 1009 Hz for the device shown in Fig. S9 and S10) was applied to the $\text{LaAlO}_3/\text{SrTiO}_3$ device. The sample was scanned over a planar SQUID sensor with a 0.8 μm diameter pick-up loop [55]. The sensor-sample distance was kept at 1 μm . The magnetic flux due to the current flow was recorded using a lock-in amplifier.

Fourier analysis was used to reconstruct the current density from the measured magnetic flux [56, 57]. First, the out of plane component of the magnetic field, $B_z(x, y)$ was recovered from the data by deconvolution with the sensor's point spread function.

The magnetic field generated by $\mathbf{J}(\mathbf{r}) = J_x(\mathbf{J})\hat{\mathbf{x}} + J_y(\mathbf{J})\hat{\mathbf{y}}$ is given by the Biot-Savart law,

$$\mathbf{B}(\mathbf{r}) = \frac{\mu_0 d}{4\pi} \int dx' \int dy' \frac{\mathbf{J}(\mathbf{r}') \times (\mathbf{r} - \mathbf{r}')}{|\mathbf{r} - \mathbf{r}'|^3}, \quad (1)$$

where μ_0 is the vacuum permeability and d is the thickness of the 2D layer. Equation 1 is a convolution integral. Therefore, the two-dimensional Fourier transform of the out-of-plane component of the magnetic field,

$$B_z(k_x, k_y, z) = \int dx \int dy B_z(x, y, z) e^{ik_x x + ik_y y}, \quad (2)$$

can be written as

$$\tilde{B}_z(k_x, k_y, z) = -i \frac{\mu_0 d}{2} e^{-|k|z} \left[\frac{k_y}{|k|} \tilde{J}_x(k_x, k_y) - \frac{k_x}{|k|} \tilde{J}_y(k_x, k_y) \right], \quad (3)$$

where $|k| = (k_x^2 + k_y^2)^{1/2}$, and \tilde{J}_x and \tilde{J}_y are the Fourier transforms of J_x and J_y , respectively. Equation 3 was used together with the continuity equation, $\mathbf{k} \cdot \tilde{\mathbf{J}} = 0$, to extract J_x and J_y from B_z . Fig. S9 shows a representative magnetic flux image recorded by the SQUID and the x and y components of the reconstructed current density. All the features seen in the reconstructed images are clearly visible in the raw data as well.

Identification of domain orientations

Domain orientations were determined by examining the tiling rules established at domain intersections. Fig. S10a shows the possible orientations of the tetragonal domain boundaries in STO, projected onto the (111) surface [39]. Each pair of domain orientations can form a boundary oriented at one of two angles with respect to the $[\bar{1}10]$ direction. For example, Fig. S10b shows a representative current density map of a device oriented 60° with respect to the $[\bar{1}10]$ direction. The current modulations reveal three types of regions: a set of narrow (10 μm) stripes of lower current density oriented along the device, the wider regions of higher current density between them, and a set of wide (30 μm) stripes with lower current density, oriented 30° with respect to $[\bar{1}10]$ direction. The orientations of these regions and the intersections between them suggest that these regions coincide with X, Y, Z tetragonal domains, respectively.

Current density simulations

To simulate the current density resulting from an anisotropic conductivity tensor, the continuity equation

$$\nabla \cdot \mathbf{J} = 0, \quad (4)$$

and Ohm's law

$$\mathbf{J} = \hat{\sigma} \mathbf{E}, \quad (5)$$

where $\hat{\sigma}$ is the conductivity tensor and \mathbf{E} is the electric field, were reformulated as a Laplace equation for the electric potential $\mathbf{E} = -\nabla V$:

$$\nabla \cdot (\hat{\sigma} \nabla V) = 0. \quad (6)$$

Equation 6 was solved for the device geometry in Fig. 1 using a finite element method. A voltage drop was set across two edges of the device, and the boundary condition $\mathbf{J} \cdot \hat{\mathbf{n}} = 0$ was applied to the rest of the edges, where $\hat{\mathbf{n}}$ is the normal to the edge.

Fig. S11 compares the expected current flow through an X-Y domain pattern in two cases: one where the conductivity is anisotropic and σ_X and σ_Y are related by a rotation, and one where the conductivity in each domain is isotropic, but its value changes between domains ($\hat{\sigma}^X = a\mathbf{1}_{2\times 2}$ and $\hat{\sigma}^Y = b\mathbf{1}_{2\times 2}$), for example due to changes to the carrier density or dielectric constant across different domains. In the latter case, the current density modulations were independent of the direction of the flow: $J_{[11\bar{2}]}$ was lower on the X domains regardless of the direction of the device.

Electrical transport measurements

The nonlinear Hall effect was measured on a Hall cross device fabricated on the same sample as used for the SQUID imaging. The sample was anchored to a chip carrier by electrically- and thermally-conductive Ag-based epoxy, and the device was electrically contacted with Al wire bonds. Four-probe measurements were performed in a liquid He⁴ cryostat at variable temperatures and magnetic fields (applied in the sample plane parallel to the electric current direction). Commercial lock-in amplifiers were used to apply an alternate current $I = 50$ μ A at a frequency $f = \omega/2\pi = 17.7$ Hz and detect the transverse first and second harmonic voltages while sweeping the magnetic field. A DC back-gate voltage was applied to tune the electronic density and mobility. The measured nonlinear Hall voltage was symmetrized and anti-symmetrized with respect to the magnetic field B to isolate distinct effects [4]. The nonlinear conductivity shown in Fig. 2c and Fig. S7 corresponds to the B -symmetric component.

Effective low-energy model

An effective model for the (111) LaAlO₃/SrTiO₃ interface was derived using the theory of invariants. We use the $|yz\rangle, |xz\rangle, |xy\rangle$ basis for the Ti t_{2g} orbitals. In the \mathcal{C}_{3v} symmetry group, there is a $2\pi/3$ rotational symmetry and one mirror plane.

Using the Gell-Mann matrices, we write the following Hamiltonian, which includes all terms, up to quadratic order, which respect the \mathcal{C}_{3v} symmetry and preserve time reversal.

$$\begin{aligned}
 H = & \epsilon_{\text{trig}}(\Lambda_3 + \Lambda_8/\sqrt{3}) + \\
 & (k_x^2 + k_y^2) \left[c_1\Lambda_0 + c_2(\Lambda_3 + \Lambda_8/\sqrt{3}) \right] + \\
 & c_4 \left[(k_x^2 - k_y^2)\Lambda_1 + 2k_xk_y\Lambda_4 \right] + \\
 & c_5 \left[(k_x^2 - k_y^2)(\Lambda_3/2 - \sqrt{3}/2\Lambda_8) + 2k_xk_y\Lambda_6 \right] + \\
 & \alpha_{\text{OR}}(k_x\Lambda_5 + k_y\Lambda_2).
 \end{aligned} \tag{7}$$

The first term is the trigonal field splitting between the a_{1g} and e_g^π bands at the Γ point. The last term is the orbital Rashba coupling, and the remaining terms account for the orbital and direction-dependent effective masses and for the trigonal warping. The prefactors were determined using the ARPES data of Ref. [38].

The tetragonal distortion reduces the symmetry group to \mathcal{C}_s by removing the rotational symmetry. This enables multiple additional terms in the Hamiltonian: splitting of the e_g^π orbitals at the Γ point, anisotropic linear terms (i.e. $k_x\Lambda_7$) and anisotropic quadratic terms (independent coefficients for the k_x^2 and k_y^2 terms). ARPES measurements do not resolve any of these contributions. To account for the anisotropy we only include a small (1 meV) splitting of the e_g^π bands.

The Hamiltonian was diagonalized analytically and the conductivity was then computed according to

$$\sigma_{\mu\nu} \sim \sum_{n=1}^3 \int d^2k \frac{\partial \epsilon_n}{\partial k_\mu} \frac{\partial \epsilon_n}{\partial k_\nu} \left(-\frac{\partial f}{\partial E} \right)_{\epsilon=\epsilon_n(\mathbf{k})}, \tag{8}$$

where $f(\epsilon)$ is the Fermi-Dirac function and we assume the relaxation time is energy independent.

SUPPLEMENTARY MATERIALS

This PDF file includes: Figs. S1 to S12.

* cortix@unisa.it

† andrea.caviglia@unige.ch

‡ beena@biu.ac.il

- [1] Yun-Yi Pai, Anthony Tylan-Tyler, Patrick Irvin, and Jeremy Levy. Physics of SrTiO₃ 3 -based heterostructures and nanostructures: a review. *Reports on Progress in Physics*, 81(3):036503, Mar 2018.
- [2] H Y Hwang, Y Iwasa, M Kawasaki, B Keimer, N Nagaosa, and Y Tokura. Emergent phenomena at oxide interfaces. *Nat. Mater.*, 11(2):103–113, Feb 2012.
- [3] Charles Ahn, Andrea Cavalleri, Antoine Georges, Sohrab Ismail-Beigi, Andrew J. Millis, and Jean-Marc Triscone. Designing and controlling the properties of transition metal oxide quantum materials. *Nat. Mater.*, 20(11):1462–1468, May 2021.
- [4] Edouard Lesne, Yildiz G. Sağlam, Raffaele Battilomo, Maria Teresa Mercaldo, Thierry C. van Thiel, Ulderico Filippozzi, Canio Noce, Mario Cuoco, Gary A. Steele, Carmine Ortix, and Andrea D. Caviglia. Designing spin and orbital sources of berry curvature at oxide interfaces. *Nat. Mater.*, 22(5):576–582, March 2023.
- [5] Maria Teresa Mercaldo, Canio Noce, Andrea D. Caviglia, Mario Cuoco, and Carmine Ortix. Orbital design of Berry curvature: pinch points and giant dipoles induced by crystal fields. *npj Quantum Mater*, 8(1):12, February 2023.
- [6] Giacomo Sala, Maria Teresa Mercaldo, Klevis Domi, Stefano Gariglio, Mario Cuoco, Carmine Ortix, and An-

- drea D. Caviglia. The quantum metric of electrons with spin-momentum locking, 2024.
- [7] N. Reyren, S. Thiel, A. D. Caviglia, L. Fitting Kourkoutis, G. Hammerl, C. Richter, C. W. Schneider, T. Kopp, A.-S. Rüetschi, D. Jaccard, M. Gabay, D. A. Muller, J.-M. Triscone, and J. Mannhart. Superconducting Interfaces Between Insulating Oxides. *Science*, 317(5842):1196–1199, Aug 2007.
 - [8] A D Caviglia, S Gariglio, N Reyren, D Jaccard, T Schneider, M Gabay, S Thiel, G Hammerl, J Mannhart, and J.-M. Triscone. Electric field control of the $\text{LaAlO}_3/\text{SrTiO}_3$ interface ground state. *Nature*, 456(7222):624–627, Dec 2008.
 - [9] B. Andrei Bernevig, Taylor L. Hughes, and Shou-Cheng Zhang. Orbitoronics: The intrinsic orbital current in p -doped silicon. *Phys. Rev. Lett.*, 95:066601, Aug 2005.
 - [10] Dongwook Go, Daegeun Jo, Hyun-Woo Lee, Mathias Kläui, and Yuriy Mokrousov. Orbitoronics: Orbital currents in solids. *EPL*, 135(3):37001, Sep 2021.
 - [11] Dongwook Go, Daegeun Jo, Changyoung Kim, and Hyun-Woo Lee. Intrinsic spin and orbital Hall effects from orbital texture. *Phys. Rev. Lett.*, 121:086602, Aug 2018.
 - [12] Seung Ryong Park, Choong H. Kim, Jaejun Yu, Jung Hoon Han, and Changyoung Kim. Orbital-angular-momentum based origin of Rashba-type surface band splitting. *Phys. Rev. Lett.*, 107:156803, Oct 2011.
 - [13] Veronika Sunko, H. Rosner, P. Kushwaha, S. Khim, F. Mazzola, L. Bawden, O. J. Clark, J. M. Riley, D. Kasinathan, M. W. Haverkort, T. K. Kim, M. Hoesch, J. Fujii, I. Vobornik, A. P. Mackenzie, and P. D. C. King. Maximal Rashba-like spin splitting via kinetic-energy-coupled inversion-symmetry breaking. *Nature*, 549(7673):492–496, Sep 2017.
 - [14] Shinobu Hikami, Anatoly I. Larkin, and Yosuke Nagaoka. Spin-orbit interaction and magnetoresistance in the two dimensional random system. *Progress of Theoretical Physics*, 63(2):707–710, 02 1980.
 - [15] J. E. Moore and J. Orenstein. Confinement-induced berry phase and helicity-dependent photocurrents. *Phys. Rev. Lett.*, 105:026805, Jul 2010.
 - [16] Inti Sodemann and Liang Fu. Quantum nonlinear Hall effect induced by berry curvature dipole in time-reversal invariant materials. *Phys. Rev. Lett.*, 115:216806, Nov 2015.
 - [17] M. Ben Shalom, C. W. Tai, Y. Lereah, M. Sachs, E. Levy, D. Rakhmilevitch, A. Palevski, and Y. Dagan. Anisotropic magnetotransport at the $\text{SrTiO}_3/\text{LaAlO}_3$ interface. *Phys. Rev. B*, 80:140403, Oct 2009.
 - [18] A. Annadi, Z. Huang, K. Gopinadhan, X. Renshaw Wang, A. Srivastava, Z. Q. Liu, H. Harsan Ma, T. P. Sarkar, T. Venkatesan, and Ariando. Fourfold oscillation in anisotropic magnetoresistance and planar hall effect at the $\text{LaAlO}_3/\text{SrTiO}_3$ heterointerfaces: Effect of carrier confinement and electric field on magnetic interactions. *Phys. Rev. B*, 87:201102, May 2013.
 - [19] Yiftach Frenkel, Noam Haham, Yishai Shperber, Christopher Bell, Yanwu Xie, Zhuoyu Chen, Yasuyuki Hikita, Harold Y Hwang, and Beena Kalisky. Anisotropic transport at the $\text{LaAlO}_3/\text{SrTiO}_3$ interface explained by microscopic imaging of channel-flow over SrTiO_3 domains. *ACS Appl. Mater. Interfaces*, 8(19):12514–12519, May 2016.
 - [20] Nicholas J Goble, Richard Akrobetu, Hicham Zaid, Sukrit Sucharitakul, Marie-Hélène Berger, Alp Sehirlioglu, and Xuan P A Gao. Anisotropic electrical resistance in mesoscopic $\text{LaAlO}_3/\text{SrTiO}_3$ devices with individual domain walls. *Sci. Rep.*, 7(1):44361, Jun 2017.
 - [21] P. W. Krantz and V Chandrasekhar. Observation of Zero-Field Transverse Resistance in $\text{AlO}_x/\text{SrTiO}_3$ Interface Devices. *Phys. Rev. Lett.*, 127(3):36801, Jul 2021.
 - [22] Mithun S Prasad and Georg Schmidt. Anisotropic magnetotransport in $\text{LaAlO}_3/\text{SrTiO}_3$ nanostructures. *Phys. Rev. B*, 104(5):054115, Aug 2021.
 - [23] Dongwook Go, Daegeun Jo, Tenghua Gao, Kazuya Ando, Stefan Blügel, Hyun-Woo Lee, and Yuriy Mokrousov. Orbital Rashba effect in a surface-oxidized cu film. *Phys. Rev. B*, 103:L121113, Mar 2021.
 - [24] Rhonald Burgos Atencia, Amit Agarwal, and Dimitrie Culcer. Orbital angular momentum of bloch electrons: equilibrium formulation, magneto-electric phenomena, and the orbital hall effect. *Advances in Physics: X*, 9(1), July 2024.
 - [25] Maria Teresa Mercaldo, Carmine Ortix, and Mario Cuoco. High orbital-moment cooper pairs by crystalline symmetry breaking. *Advanced Quantum Technologies*, 6(8):2300081, 2023.
 - [26] Beena Kalisky, Eric M Spanton, Hilary Noad, John R Kirtley, Katja C Nowack, Christopher Bell, Hiroki K Sato, Masayuki Hosoda, Yanwu Xie, Yasuyuki Hikita, Carsten Woltmann, Georg Pfanzelt, Rainer Jany, Christoph Richter, Harold Y Hwang, Jochen Mannhart, and Kathryn A Moler. Locally enhanced conductivity due to the tetragonal domain structure in $\text{LaAlO}_3/\text{SrTiO}_3$ heterointerfaces. *Nat. Mater.*, 12(12):1091–1095, Dec 2013.
 - [27] M Honig, J A Sulpizio, J Drori, A Joshua, E Zeldov, and S Ilani. Local electrostatic imaging of striped domain order in $\text{LaAlO}_3/\text{SrTiO}_3$. *Nat. Mater.*, 12(12):1112–1118, Dec 2013.
 - [28] H. J. Harsan Ma, S. Scharinger, S. W. Zeng, D. Kohlberger, M. Lange, A. Stöhr, X. Renshaw Wang, T. Venkatesan, R. Kleiner, J. F. Scott, J. M. D. Coey, D. Koelle, and Ariando. Local electrical imaging of tetragonal domains and field-induced ferroelectric twin walls in conducting SrTiO_3 . *Phys. Rev. Lett.*, 116:257601, Jun 2016.
 - [29] Hilary Noad, Eric M Spanton, Katja C Nowack, Hisashi Inoue, Minu Kim, Tyler A Merz, Christopher Bell, Yasuyuki Hikita, Ruqing Xu, Wenjun Liu, Arturas Vailionis, Harold Y Hwang, and Kathryn A Moler. Variation in superconducting transition temperature due to tetragonal domains in two-dimensionally doped SrTiO_3 . *Phys. Rev. B*, 94(17):174516, Nov 2016.
 - [30] Shai Wissberg and Beena Kalisky. Large-scale modulation in the superconducting properties of thin films due to domains in the SrTiO_3 substrate. *Phys. Rev. B*, 95(14):144510, Apr 2017.
 - [31] Eylon Persky, Naor Vardi, Ana Mafalda R V L Monteiro, Thierry C. van Thiel, Hyeok Yoon, Yanwu Xie, Benoît Fauqué, Andrea D. Caviglia, Harold Y. Hwang, Kamran Behnia, Jonathan Ruhman, and Beena Kalisky. Non-universal current flow near the metal-insulator transition in an oxide interface. *Nat. Commun.*, 12(1):3311, Dec 2021.
 - [32] Yiftach Frenkel, Noam Haham, Yishai Shperber, Christopher Bell, Yanwu Xie, Zhuoyu Chen, Yasuyuki Hikita,

- Harold Y Hwang, Ekhard K H Salje, and Beena Kalisky. Imaging and tuning polarity at SrTiO_3 domain walls. *Nat. Mater.*, 16(12):1203–1208, 2017.
- [33] Guanglei Cheng, Anil Annadi, Shicheng Lu, Hyungwoo Lee, Jung-Woo Lee, Mengchen Huang, Chang-Beom Eom, Patrick Irvin, and Jeremy Levy. Shubnikov-de Haas-like Quantum Oscillations in Artificial One-Dimensional $\text{LaAlO}_3/\text{SrTiO}_3$ Electron Channels. *Phys. Rev. Lett.*, 120(7):76801, Dec 2018.
- [34] Yun-Yi Pai, Hyungwoo Lee, Jung-Woo Lee, Anil Annadi, Guanglei Cheng, Shicheng Lu, Michelle Tomczyk, Mengchen Huang, Chang-Beom Eom, Patrick Irvin, and Jeremy Levy. One-dimensional nature of superconductivity at the $\text{LaAlO}_3/\text{SrTiO}_3$ interface. *Phys. Rev. Lett.*, 120(14):147001, Apr 2018.
- [35] K A Müller and H Burkard. SrTiO_3 : An intrinsic quantum paraelectric below 4 K. *Phys. Rev. B*, 19(7):3593–3602, Apr 1979.
- [36] Hang-Bo Zhang and Marin Alexe. Interfacial symmetry-breaking effects in the quantum paraelectric SrTiO_3 . *Phys. Rev. Appl.*, 19:014028, Jan 2023.
- [37] Valentina Brosco, Lara Benfatto, Emmanuele Cappelluti, and Claudio Grimaldi. Unconventional dc transport in Rashba electron gases. *Phys. Rev. Lett.*, 116:166602, Apr 2016.
- [38] T. C. Rödel, C. Bareille, F. Fortuna, C. Baumier, F. Bertran, P. Le Fèvre, M. Gabay, O. Hijano Cubelos, M. J. Rozenberg, T. Maroutian, P. Lecoeur, and A. F. Santander-Syro. Orientational tuning of the fermi sea of confined electrons at the SrTiO_3 (110) and (111) surfaces. *Phys. Rev. Applied*, 1:051002, Jun 2014.
- [39] Petr S Bednyakov, Tomas Sluka, Alexander K Tagantsev, Dragan Damjanovic, and Nava Setter. Formation of charged ferroelectric domain walls with controlled periodicity. *Sci. Rep.*, 5(1):15819, Dec 2015.
- [40] S. McKeown Walker, A. de la Torre, F. Y. Bruno, A. Tamai, T. K. Kim, M. Hoesch, M. Shi, M. S. Bahramy, P. D. C. King, and F. Baumberger. Control of a two-dimensional electron gas on SrTiO_3 (111) by atomic oxygen. *Phys. Rev. Lett.*, 113:177601, Oct 2014.
- [41] A. F. Santander-Syro, C. Bareille, F. Fortuna, O. Copie, M. Gabay, F. Bertran, A. Taleb-Ibrahimi, P. Le Fèvre, G. Herranz, N. Reyren, M. Bibes, A. Barthélémy, P. Lecoeur, J. Guevara, and M. J. Rozenberg. Orbital symmetry reconstruction and strong mass renormalization in the two-dimensional electron gas at the surface of KTaO_3 . *Phys. Rev. B*, 86:121107, Sep 2012.
- [42] P. D. C. King, R. H. He, T. Eknepakul, P. Buaphet, S.-K. Mo, Y. Kaneko, S. Harashima, Y. Hikita, M. S. Bahramy, C. Bell, Z. Hussain, Y. Tokura, Z.-X. Shen, H. Y. Hwang, F. Baumberger, and W. Meevasana. Subband structure of a two-dimensional electron gas formed at the polar surface of the strong spin-orbit perovskite KTaO_3 . *Phys. Rev. Lett.*, 108:117602, Mar 2012.
- [43] A D Caviglia, M Gabay, S Gariglio, N Reyren, C Cancellieri, and J.-M. Triscone. Tunable Rashba Spin-Orbit Interaction at Oxide Interfaces. *Phys. Rev. Lett.*, 104(12):126803, Mar 2010.
- [44] M Ben Shalom, M Sachs, D Rakhmilevitch, A Palevski, and Y Dagan. Tuning Spin-Orbit Coupling and Superconductivity at the $\text{SrTiO}_3/\text{LaAlO}_3$ Interface: A Magnetotransport Study. *Phys. Rev. Lett.*, 104(12):126802, Mar 2010.
- [45] Arjun Joshua, S Pecker, J Ruhman, E Altman, and S Ilani. A universal critical density underlying the physics of electrons at the $\text{LaAlO}_3/\text{SrTiO}_3$ interface. *Nat. Commun.*, 3(1), 2012.
- [46] P. K. Rout, E Maniv, and Y Dagan. Link between the Superconducting Dome and Spin-Orbit Interaction in the (111) $\text{LaAlO}_3/\text{SrTiO}_3$ Interface. *Phys. Rev. Lett.*, 119(23):237002, Dec 2017.
- [47] A M R V L Monteiro, M Vivek, D J Groenendijk, P Bruneel, I Leermakers, U Zeitler, M Gabay, and A D Caviglia. Band inversion driven by electronic correlations at the (111) $\text{LaAlO}_3/\text{SrTiO}_3$ interface. *Phys. Rev. B*, 99(20):201102, May 2019.
- [48] Francesco Casola, Toeno van der Sar, and Amir Yacoby. Probing condensed matter physics with magnetometry based on nitrogen-vacancy centres in diamond. *Nat. Rev. Mater.*, 3:17088, Jan 2018.
- [49] Lior Ella, Asaf Rozen, John Birkbeck, Moshe Ben-Shalom, David Perello, Johanna Zultak, Takashi Taniguchi, Kenji Watanabe, Andre K. Geim, Shahal Ilani, and Joseph A. Sulpizio. Simultaneous voltage and current density imaging of flowing electrons in two dimensions. *Nat. Nanotechnol.*, 14(5):480–487, Mar 2019.
- [50] P. Muralt and D. W. Pohl. Scanning tunneling potentiometry. *Appl. Phys. Lett.*, 48(8):514–516, 02 1986.
- [51] J. Martin, N. Akerman, G. Ulbricht, T. Lohmann, J. H. Smet, K. von Klitzing, and A. Yacoby. Observation of electron-hole puddles in graphene using a scanning single-electron transistor. *Nat. Phys.*, 4(2):144–148, Nov 2007.
- [52] J. Waissman, M. Honig, S. Pecker, A. Benyamini, A. Hamo, and S. Ilani. Realization of pristine and locally tunable one-dimensional electron systems in carbon nanotubes. *Nat. Nanotechnol.*, 8(8):569–574, Aug 2013.
- [53] Giacomo Sala, Hanchen Wang, William Legrand, and Pietro Gambardella. Orbital hantle magnetoresistance in a 3d transition metal. *Phys. Rev. Lett.*, 131:156703, Oct 2023.
- [54] Young-Gwan Choi, Daegeun Jo, Kyung-Hun Ko, Dongwook Go, Kyung-Han Kim, Hee Gyum Park, Changyoung Kim, Byoung-Chul Min, Gyung-Min Choi, and Hyun-Woo Lee. Observation of the orbital Hall effect in a light metal Ti. *Nature*, 619(7968):52–56, July 2023.
- [55] Martin E. Huber, Nicholas C. Koshnick, Hendrik Bluhm, Leonard J. Archuleta, Tommy Azua, Per G. Björnsson, Brian W. Gardner, Sean T. Halloran, Erik A. Lucero, and Kathryn A. Moler. Gradiometric micro-squid susceptometer for scanning measurements of mesoscopic samples. *Rev. Sci. Instrum.*, 79(5):053704, 05 2008.
- [56] Bradley J Roth, Nestor G Sepulveda, and John P Wikswo. Using a magnetometer to image a two-dimensional current distribution. *J. Appl. Phys.*, 65(1):361–372, Jan 1989.
- [57] Katja C Nowack, Eric M Spanton, Matthias Baenninger, Markus König, John R Kirtley, Beena Kalisky, C Ames, Philipp Leubner, Christoph Brüne, Hartmut Buhmann, Laurens W Molenkamp, David Goldhaber-Gordon, and Kathryn A Moler. Imaging currents in HgTe quantum wells in the quantum spin Hall regime. *Nat. Mater.*, 12(9):787–791, 2013.

Acknowledgments: E.P., X.W. and B.K. were supported by the European Research Council Grant No.

ERC-2019-COG-866236, the Israeli Science Foundation, grant no. ISF-228/22, COST Action CA21144, and the Pazy Research Foundation grant no. 107-2018. G.S. acknowledges support from the Swiss National Science Foundation (grant no. PZ00P2_223542). A.L. was supported by a Marie Skłodowska-Curie Individual Fellowship under grant MagTopCSL (ID 101029345) and by the Foundation for Polish Science through the IRA Programme co-financed by EU within SG OP. C.O. acknowledges support from a VIDI grant (Project 680-47-543) financed by the Netherlands Organization for Scientific Research (NWO). E.L. acknowledges funding from the EU Horizon 2020 research and innovation programme under the Marie Skłodowska-Curie grant agreement no.

707404. **Author contributions:** E.P., X.W. and B.K. designed and conducted the scanning SQUID experiments and finite element simulations. G.S. conducted the non-linear transport measurements. T.C.v.T. and E.L. fabricated and patterned the sample. A.L. and C.O. proposed the theoretical model. E.P, A.L. and C.O. performed the band structure calculations. E.P., X.W., C.O., A.D.C and B.K. discussed and interpreted the results with contributions from all co-authors. E.P., C.O., A.D.C and B.K. wrote the manuscript with input from all coauthors. **Competing interests:** The authors declare that they have no competing interests. **Data availability:** The raw data are available from the corresponding authors upon reasonable request.

SUPPLEMENTAL MATERIAL FOR Imaging orbital Rashba induced charge transport anisotropy

Eylon Persky,^{1,2} Xi Wang,^{1,2} Giacomo Sala,³ Thierry C. van Thiel,⁴ Edouard Lesne,^{4,5} Alexander Lau,⁶ Mario Cuoco,⁷ Marc Gabay,⁸ Carmine Ortix,^{9*} Andrea D. Caviglia,^{3†} and Beena Kalisky^{1,2‡}

¹*Department of Physics, Bar-Ilan University, Ramat-Gan 5290002, Israel*

²*Institute of Nanotechnology and Advanced Materials, Bar-Ilan University, Ramat-Gan 5290002, Israel*

³*Department of Quantum Matter Physics, University of Geneva, 24 Quai Ernest Ansermet, CH-1211 Geneva, Switzerland*

⁴*Kavli Institute of Nanoscience, Delft University of Technology, Lorentzweg 1, 2628CJ Delft, Netherlands*

⁵*Max Planck Institute for Chemical Physics of Solids, 01187 Dresden, Germany*

⁶*International Research Centre MagTop, Institute of Physics, Polish Academy of Sciences, Aleja Lotników 32/46, PL-02668 Warsaw, Poland*

⁷*Consiglio Nazionale delle Ricerche, CNR-SPIN, Italy*

⁸*Laboratoire de Physique des Solides, Université Paris-Saclay, CNRS UMR 8502, Orsay, France*

⁹*Dipartimento di Fisica "E. R. Caianiello", Università di Salerno, IT-84084 Fisciano, Italy*

*cortix@unisa.it, †andrea.caviglia@unige.ch, ‡beena@biu.ac.il

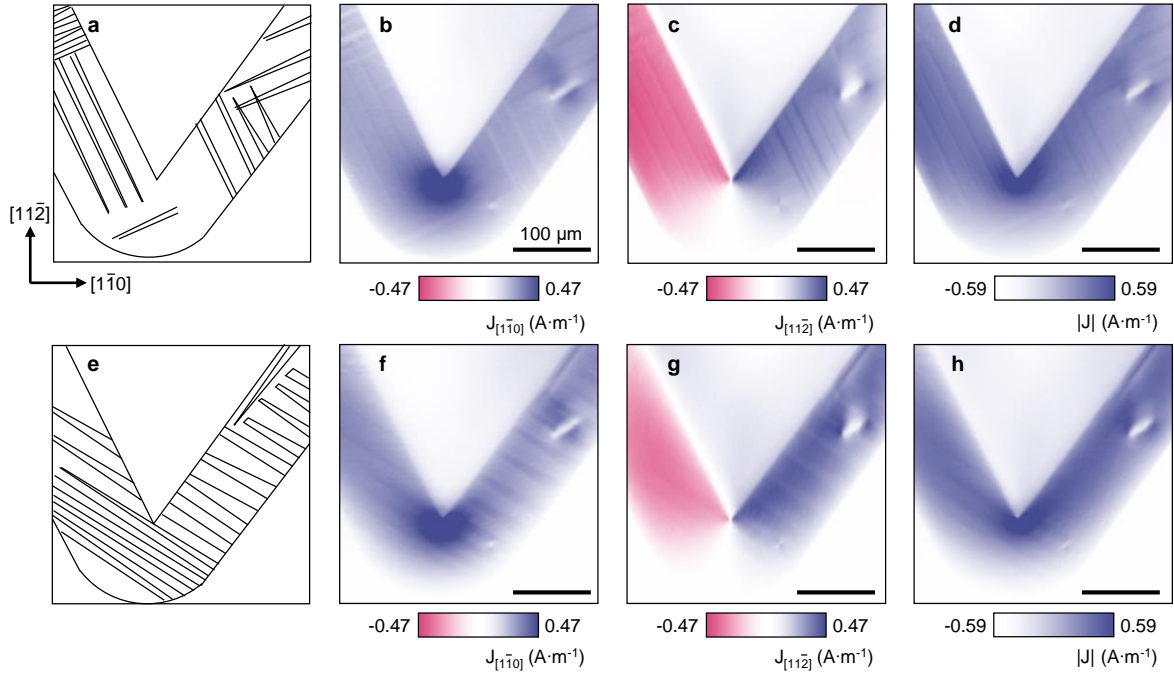


FIG. S1: Different domain patterns by thermal cycling. (a-d) Current flowing in a v-shape device with Y-Z domain patterns. (a) Sketch of domain patterns. (b-d) Inverted current density for $J_{[110]}$, $J_{[112]}$, and $|J|$. (e-h) Current flowing in the same device but with X-Z domain patterns. Between these two sets of images, the temperature was cycled to 300 K.

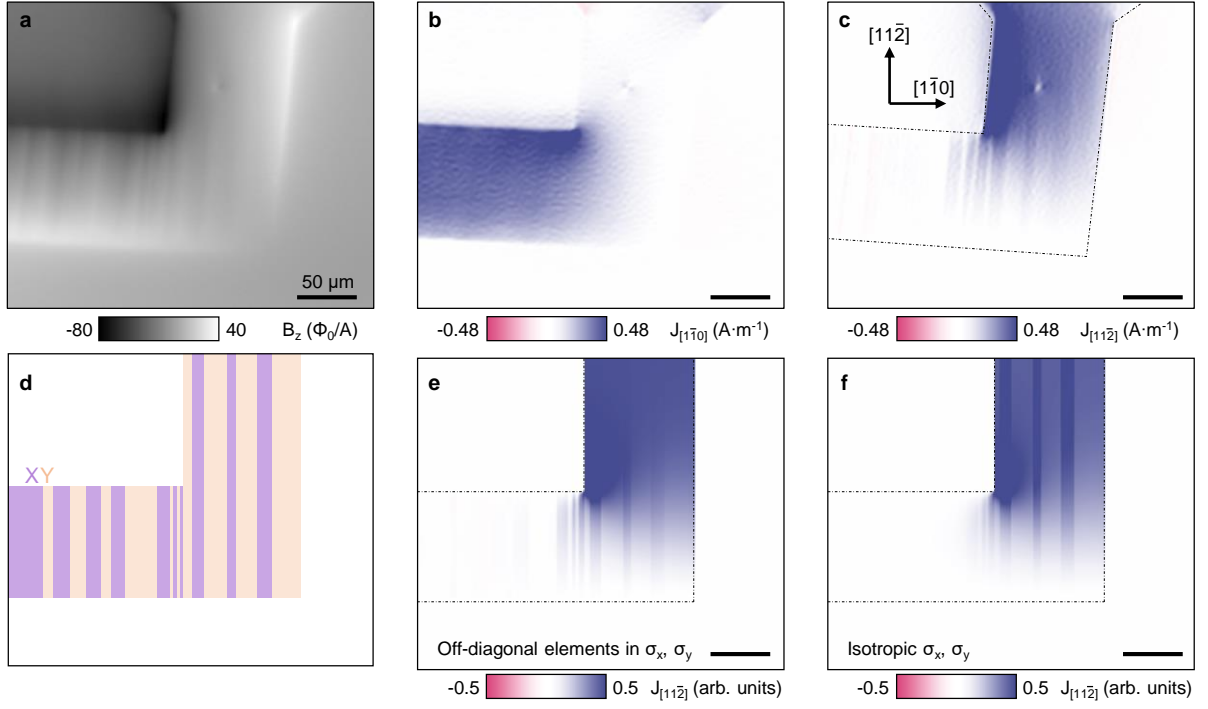


FIG. S2: Additional examples of changes in the modulations by reflecting the direction of current. (a) Raw magnetic flux data from an applied current of $40 \mu\text{A}$ RMS. (b,c) The reconstructed $[1\bar{1}0]$ (b) and $[11\bar{2}]$ (c) components of the current density. (d) The expected XY domain configuration of this device. (e,f) The finite element simulations by using anisotropic conductivity (e) and isotropic conductivity (f). In panel f, the conductivity of X domains is set to be 20% higher than Y domains.

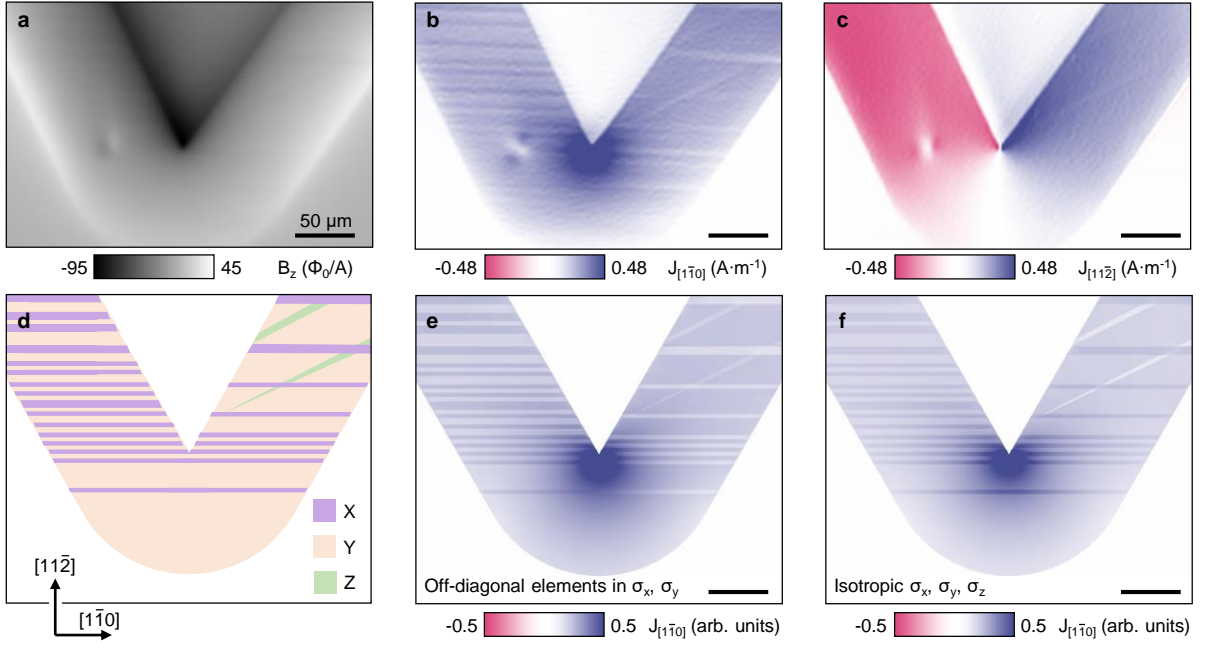


FIG. S3: Additional examples of changes in the modulations by reflecting the direction of current. This is the same device shown in Fig. 1 but the patterns are different due to a thermal cycle to 300 K. (a) Raw magnetic flux data from an applied current of $40 \mu\text{A}$ RMS. (b,c) The reconstructed $[1\bar{1}0]$ (b) and $[11\bar{2}]$ (c) components of the current density. (d) The expected XYZ domain configuration of this device. (e,f) The finite element simulations by using anisotropic conductivity (e) and isotropic conductivity (f). In panel f, the conductivity of X and Z domains is set to be 20% higher or weaker than Y domains.

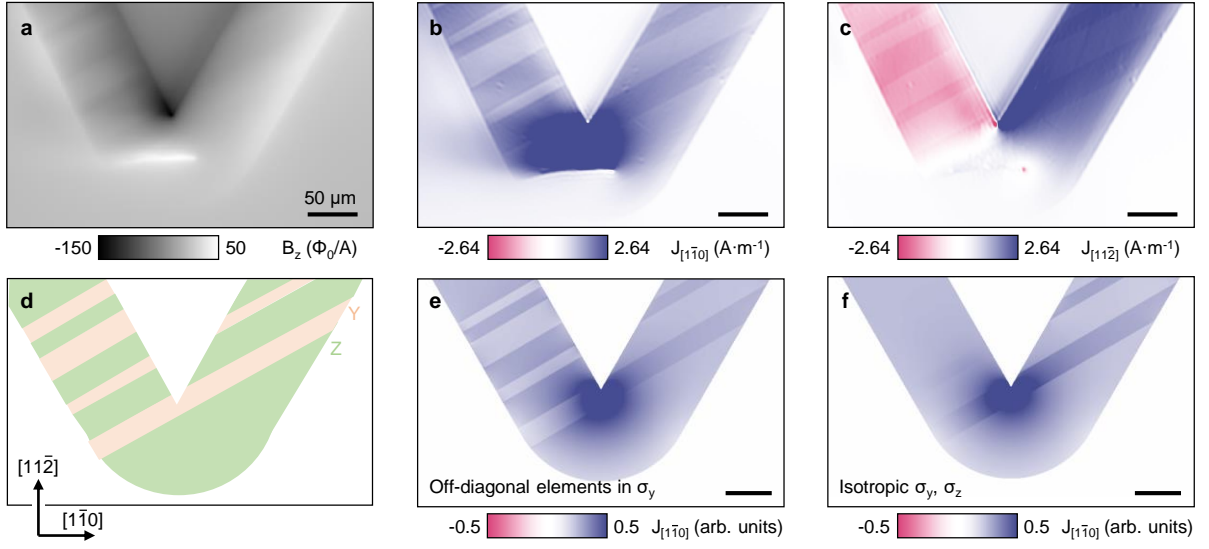


FIG. S4: Additional examples of changes in the modulations by reflecting the direction of current. (a) Raw magnetic flux data from an applied current of $264 \mu\text{A}$ RMS. (b,c) The reconstructed $[1\bar{1}0]$ (b) and $[11\bar{2}]$ (c) components of the current density. (d) The expected YZ domain configuration of this device. (e,f) The finite element simulations by using anisotropic conductivity (e) and isotropic conductivity (f). In panel f, the conductivity of Y domains is set to be 20% higher than Z domains.

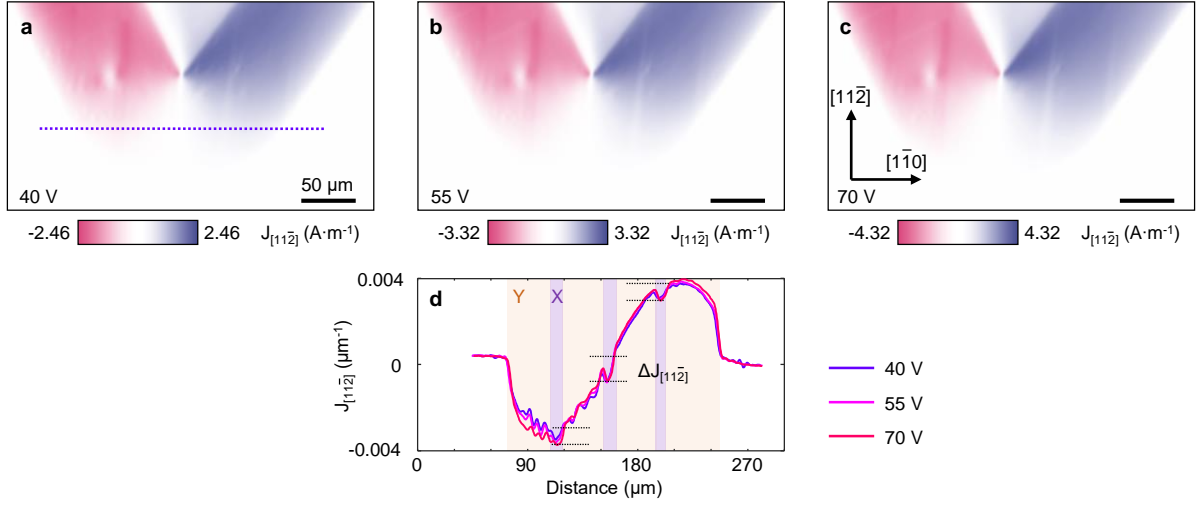


FIG. S5: Gate dependence of $J_{[11\bar{2}]}$ in the device shown in Fig. 1 at 7 K. (a-c) From the gate voltage of 40 to 70 V, the relevant currents are 205, 277, 360 μA , correspondingly. The modulation amplitudes of these three images are plotted in Fig. 3f, light orange color. We used a constant voltage bias setup with a lock-in amplifier, accounting for this change in current with the gate voltage. The data is normalized by the applied current. (d) Line cuts taken from panels a, b, and c. The data is normalized by the applied current.

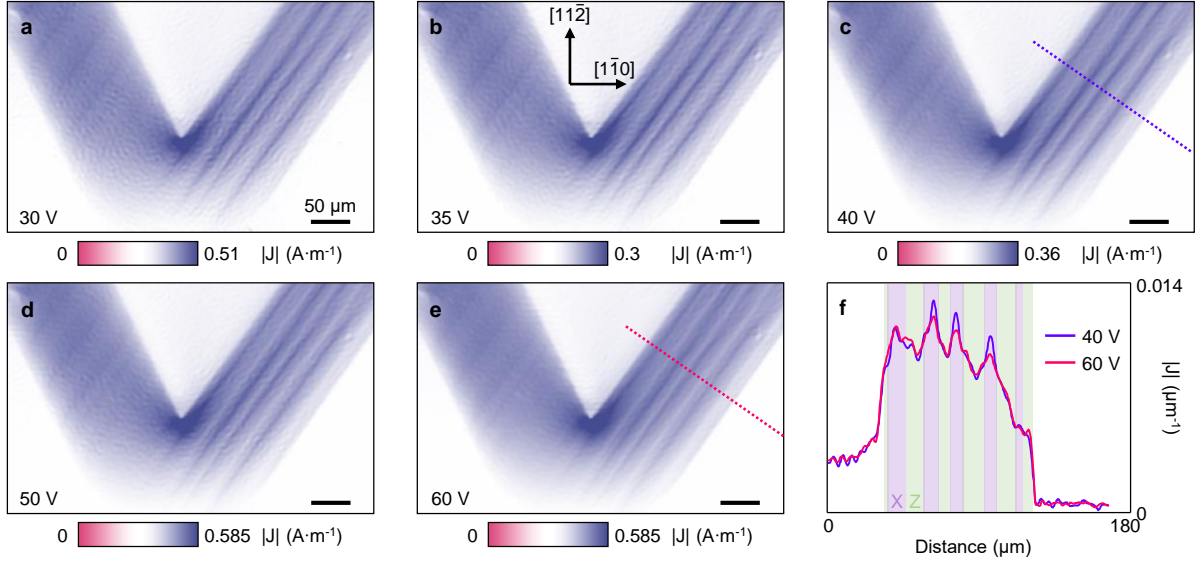


FIG. S6: Gate dependence of $|J|$ at 5.5 K, in the device shown in the Extended Data Fig. S9 and S10. (a-e) From the gate voltage of 30 to 60 V, the relevant currents are 34, 20, 24, 39, 39 μA , correspondingly. The modulation amplitudes of these XZ domain structures are plotted in Fig. 3f, dark blue color. (f) Line cuts taken from panels c and e. The modulation at 40 V is slightly stronger than at 60 V. The data is normalized by the applied current.

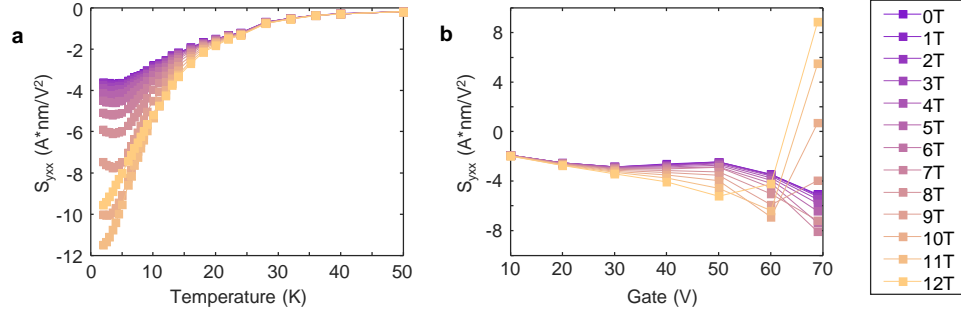


FIG. S7: Magnetotransport data. (a) Temperature and (b) gate dependence of the non-linear conductivity up to 12 T, showing similar onset temperature to the anisotropy, and a non-monotonic dependence on the gate voltage. The data at zero field is presented in the main text Fig. 2 panels c and e.

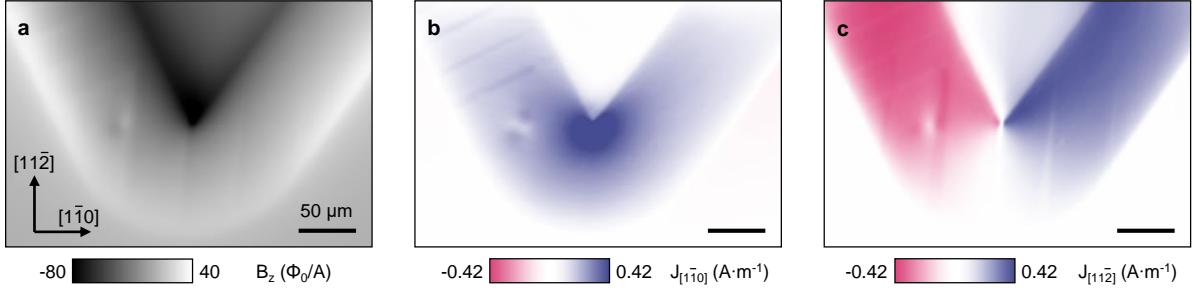


FIG. S8: Current density reconstruction of the device shown in Fig. 1 at gate voltage 70 V. (a) Raw magnetic flux data due to an applied current of $34\ \mu\text{A}$ RMS in a $100\ \mu\text{m}$ wide (111)-LAO/STO device. (b,c) The reconstructed $[1\bar{1}0]$ (b) and $[11\bar{2}]$ (c) components of the current density.

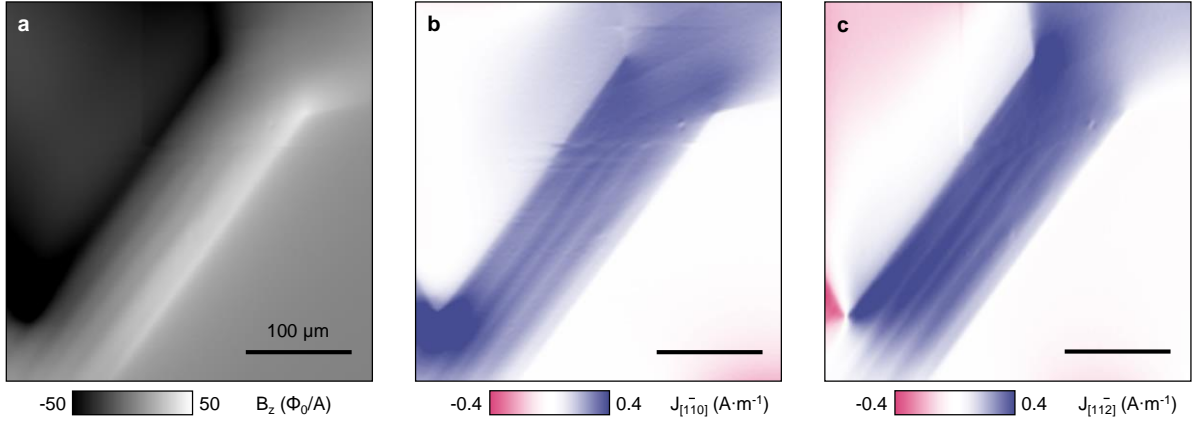


FIG. S9: Current density reconstruction. (a) Raw magnetic flux data due to an applied current of $40\mu\text{A}$ RMS in a $100\mu\text{m}$ wide (111)-LAO/STO device. (b,c) The reconstructed $[1\bar{1}0]$ (b) and $[11\bar{2}]$ (c) components of the current density. All data are normalized by the applied current.

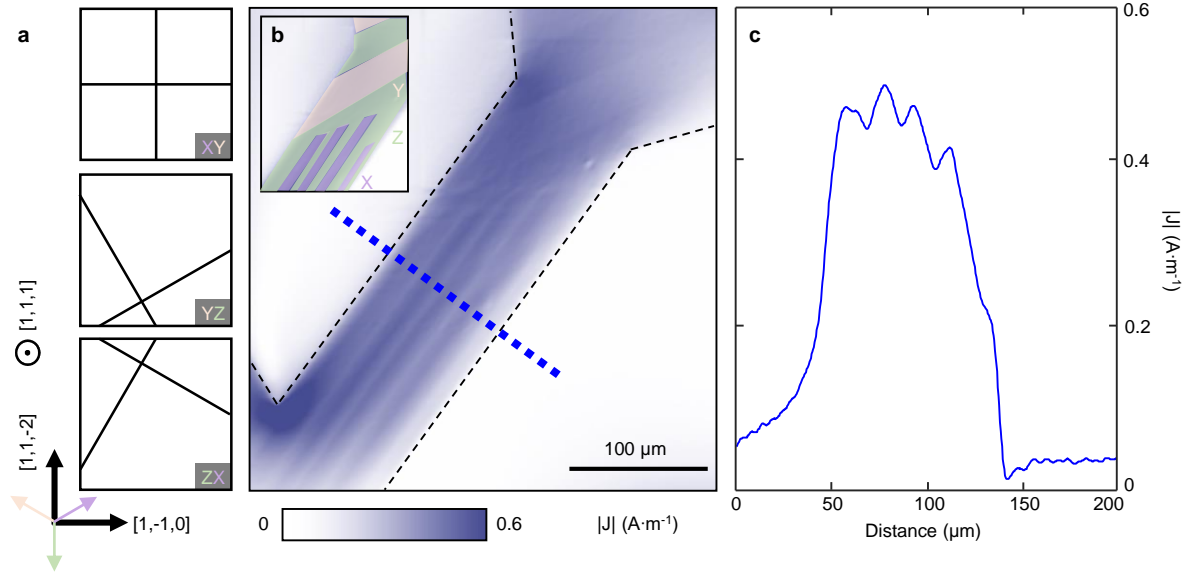


FIG. S10: Tetragonal domain patterns in (111) LAO/STO. (a) domain walls projected onto the (111) oriented surface. Boundaries between X and Y domains form 0° and 90° with respect to the $[1\bar{1}0]$ direction, Y-Z boundaries form 30° and 120° and X-Z boundaries form 60° and 150° . (b) A representative current density image of a patterned (111) LAO/STO device, showing modulations along wide stripes oriented 30° and 60° . Inset: From these orientations, we infer the structural domain configuration in this area. The black dashed lines mark the edges of the device. (c) Line cut of the current density taken along the blue dashed line in b, showing the X-Z domain pattern causes a current density modulation of 11%.

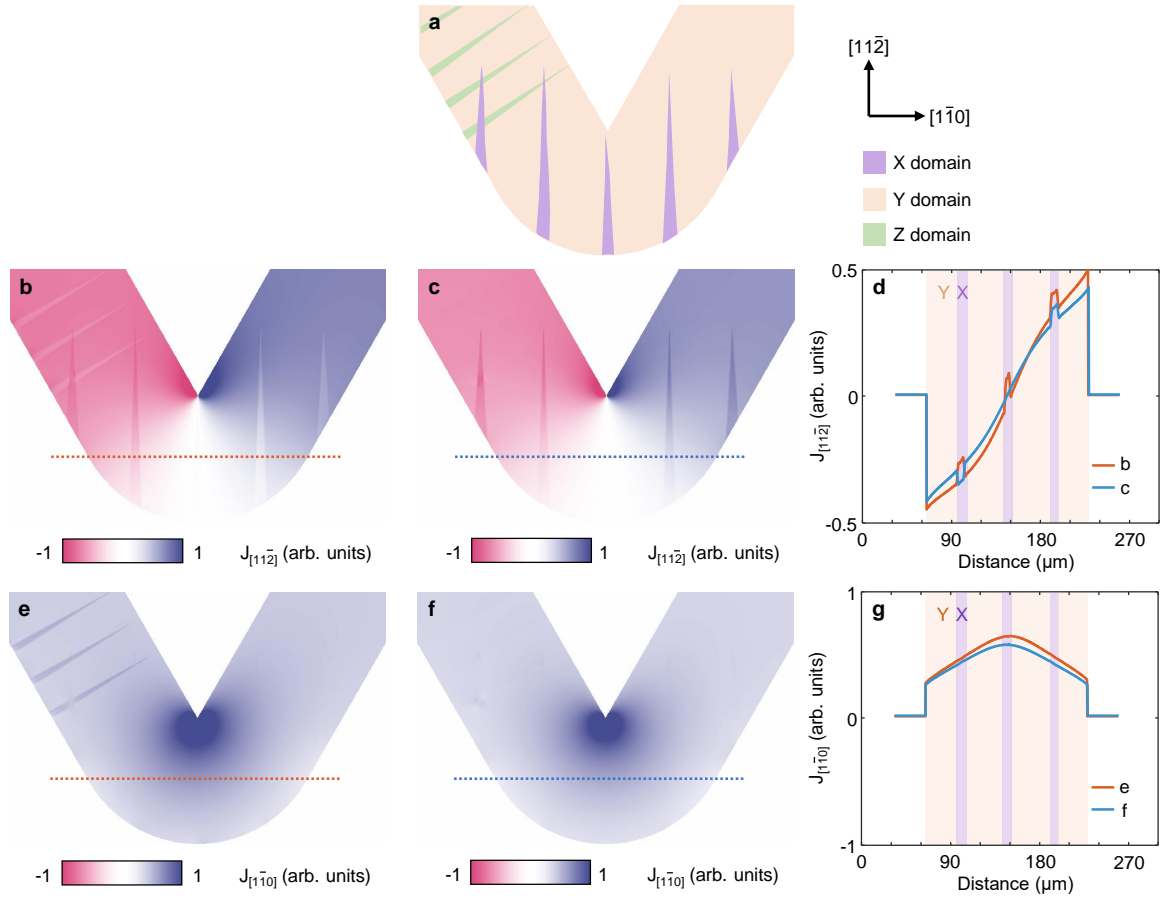


FIG. S11: Finite element simulations of current flow in a triangle shape device with an X-Y domain pattern. (a) The domain patterns. (b) The modulations in $J_{[11\bar{2}]}$ are caused by anisotropic conductivity. (c) The modulations are caused by different isotropic conductivities in the different domains. Note that the latter scenario does not reproduce the reversed modulations observed in the experiment or the modulation in Z domains. (d) Line cuts from the current density maps in panels b, c. (e) Simulation results with anisotropic conductivity in $J_{[1\bar{1}0]}$ component of panels a, b where the X-Y domain modulation is barely visible. (f) In the simulation of different isotropic conductivities, the modulation in Z domains is not visible as well. (g) Line cuts from the current density maps in panels e, f.

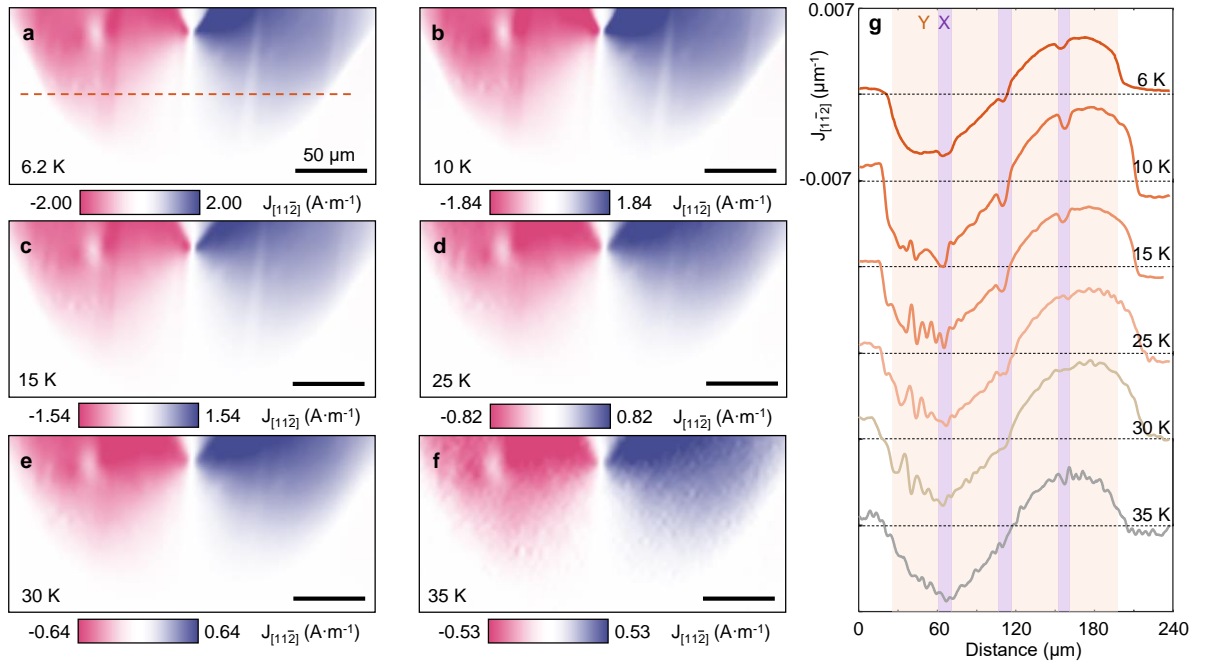


FIG. S12: Temperature dependence of $J_{[11\bar{2}]}$ in the device shown in Fig. 1 at gate voltage 70 V. (a-f) From 6 to 35 K, the amplitudes of current are 167, 153, 128, 68, 53, 44 μ A, correspondingly. We used a constant voltage bias setup with a lock-in amplifier, accounting for the change of current with temperatures. (g) Line cuts taken from panels a-f. At 35 K the modulation is beyond our sensitivity. The data is normalized by the applied current.